catalysts

MDPI

Article

Hydrothermal Synthesis of Bimetallic (Zn, Co) Co-Doped Tungstate Nanocomposite with Direct Z-Scheme for Enhanced Photodegradation of Xylenol Orange

Fahad A. Alharthi *, Wedyan Saud Al-Nafaei, Alanoud Abdullah Alshayiqi, Hamdah S. Alanazi and Imran Hasan *

Department of Chemistry, College of Science, King Saud University, Riyadh 11451, Saudi Arabia
* Correspondence: fharthi@ksu.edu.sa (F.A.A.); iabdulateef@ksu.edu.sa (I.H.)

Abstract: In the present study, pristine $ZnWO_4$, $CoWO_4$, and mixed metal $Zn_{0.5}Co_{0.5}WO_4$ were synthesized through the hydrothermal process using a Teflon-lined autoclave at 180 °C. The synthesized nanomaterials were characterized by various spectroscopic techniques, such as TEM, FTIR, UV–vis, XRD, and SEM-EDX-mapping to confirm the formation of nanocomposite material. The synthesized materials were explored as photocatalysts for the degradation of xylenol orange (XO) under a visible light source and a comparative study was explored to check the efficiency of the bimetallic co-doped nanocomposite to the pristine metal tungstate NPs. XRD analysis proved that reinforcement of Co^{2+} in $ZnWO_4$ lattice results in a reduction in interplanar distance from 0.203 nm to 0.185 nm, which is reflected in its crystallite size, which reduced from 32 nm to 24 nm. Contraction in crystallite size reflects on the optical properties as the energy bandgap of $ZnWO_4$ reduced from 3.49 eV to 3.33 eV in $Zn_{0.5}Co_{0.5}WO_4$, which is due to the formation of a Z-scheme for charge transfer and enhancement in photocatalytic efficiency. The experimental results suggested that $ZnWO_4$, $CoWO_4$, and $Zn_{0.5}Co_{0.5}WO_4$ NPs achieved a photocatalytic efficiency of 97.89%, 98.10%, and 98.77% towards XO in 120 min of visible solar light irradiation. The kinetics of photodegradation was best explained by pseudo-first-order kinetics and the values of apparent rate const (k_{app}) also supported the enhanced photocatalytic efficiency of mixed metal $Zn_{0.5}Co_{0.5}WO_4$ NPs towards XO degradation.

Keywords: nanocomposites; bimetallic Z-scheme; photoreduction; hydrothermal reaction; organic pollutants

check for updates

Citation: Alharthi, F.A.; Al-Nafaei, W.S.; Alshayiqi, A.A.; Alanazi, H.S.; Hasan, I. Hydrothermal Synthesis of Bimetallic (Zn, Co) Co-Doped Tungstate Nanocomposite with Direct Z-Scheme for Enhanced Photodegradation of Xylenol Orange. *Catalysts* **2023**, *13*, 404. https://doi.org/10.3390/catal13020404

Academic Editor: Meng Li

Received: 13 December 2022
Revised: 15 January 2023
Accepted: 17 January 2023
Published: 14 February 2023

Copyright: © 2023 by the authors. Licensee MDPI, Basel, Switzerland. This article is an open access article distributed under the terms and conditions of the Creative Commons Attribution (CC BY) license (https://creativecommons.org/licenses/by/4.0/).

1. Introduction

The development of societies and industries has led to the deterioration of freshwater qualities through the release of untreated effluents containing hazardous chemical contaminants, such as dyes and pharmaceutical products, etc. [1,2]. The toxic organic compounds, especially dyes and pharmaceuticals, contaminated wastewater in the environment, which can cause a variety of health issues to humans [3,4]. Among various organic pollutants, xylenol orange (XO; $C_{31}H_{32}N_2O_{13}S$) belongs to the acidic dye family commonly used in the textile, paper, and printing industries, but beyond the permissible limit, it causes nervous system breakdown, liver–kidney damage, blood disorders, and skin irritation [5,6]. So, it has become a matter of serious concern to develop new technology-based methods and resolutions which can treat these hazardous chemicals in the water and regulate their limits in the aquatic environment. Among various chemical, physical, and biological wastewater treatment methods, photocatalysis enables the adsorbed organic molecules to be degraded at a low cost into H_2O and CO_2 using solar irradiation, which is abundant, renewable, and environmentally friendly [7,8]. Moreover, advanced oxidation processes (AOPs) were created to promote the removal or degradation of contaminant species through redox processes, focused on the remediation of contaminants in wastewater; they are a group of techniques that use reactive oxidant species (ROS) to mineralize a wide range of resistant organics [9,10].

Metal tungstate nanoparticles (NPs) have received a lot of interest among the different types of semiconductor photocatalysts [11]. For this reason, the study and synthesis of single photocatalysts that successfully use visible light to stimulate photocatalysis have recently become a promising idea. Until now, various semiconductors with sufficient energy band gaps to absorb visible light, such as Fe_2O_3, Ag_2O, Bi_2WO_6, g-C_3N_4, $MnWO_4$, $CdWO_4$, CdS, $NiMoO_4$, Cu_2O, ln_2S_3, and Si_3N_4, have been effectively synthesized and utilized for photocatalysis, because of its high average refractive index, high chemical stability, excellent light absorbing property, and high catalytic activity [12–14]. In the tungstate family, zinc tungstate ($ZnWO_4$) has been a widely known semiconductor photocatalyst owing to its high physical and chemical stability and difficulty to dissolve [15]. However, due to homogeneity, it is only UV light active and possesses a high rate of electron–hole pair recombination, which poses an obstacle in the practical applications of $ZnWO_4$ [16]. Various methods have been applied previously to increase the photocatalytic efficiency of $ZnWO_4$, such as semiconductor coupling [17], noble metal loading [18], and metal deposition [19]. The metal deposition of $ZnWO_4$ with other metals having a narrow band gap could effectively inhibit the electron–hole pair recombination by expanding the light absorption range, and thus a robust enhancement in photocatalytic efficiency will appear [20,21]. So, the Co deposition method was applied in this study to synthesize the Co-doped nanocomposite $Zn_{0.5}Co_{0.5}WO_4$ with improved energy bandgap, optical properties (UV–vis light active), and photocatalytic efficiency. Since the ionic radii of both Co^{2+} and Zn^{2+} are approximately the same, it can be easily deposited in the solid matrix of $ZnWO_4$ and result in the reduction of the energy bandgap from 3.87 eV ($ZnWO_4$) to 1.95 eV ($Zn_{0.5}Co_{0.5}WO_4$). $ZnWO_4$ was identified as a large band gap semiconductor (band gap = 3.87 eV) with the appropriate conduction band and valance band locations based on its electronic characteristics, while, on the other hand, cobalt tungstate ($CoWO_4$) has been recognized as having excellent phase composition, strong chemical stability, and a low energy bandgap, which makes it adaptable to degrade the dyestuff in the visible light range [22].

In the present work, a hydrothermal method was used for the synthesis of pristine metal tungstate nanomaterials ($ZnWO_4$, $CoWO_4$ NPs) and mixed metal tungstate nanocomposite ($Zn_{0.5}Co_{0.5}WO_4$ NPs) using a Teflon line autoclave. The synthesized NPs were explored for the photocatalytic degradation of XO dye and a comparative study was designed to explore the photocatalytic mechanism and efficiency of the photocatalyst.

2. Results and Discussion

2.1. Material Characterization

Figure 1 represents the FTIR of $ZnWO_4$, $CoWO_4$, and $Zn_{0.5}Co_{0.5}WO_4$, in which the characteristic peaks of $ZnWO_4$ are 3448 and 1644 cm^{-1} (stretching and bending vibrations of –OH group) due to surface adsorbed water, 473 to 881 cm^{-1} (W_2O_8 bonds (WO_6) groups shared at edges and WO_2 groups), and 473 cm^{-1} (stretching vibrational of the Zn–O) [23]. Three peaks at 541, 685, and 716 cm^{-1} correspond to symmetric and asymmetric stretching vibrations of the bridging atom of the WO_2 groups of distorted octahedral (WO_6) clusters [24]. Broad absorption bands at 816 cm^{-1} and 881 cm^{-1} are caused by symmetrical vibrations of bridge oxygen atoms of Zn–O–W groups [24]. Similar types of stretching and vibrational bands are also shown by $CoWO_4$ with different peak values and 469 cm^{-1} belongs to the Co–O bond. As compared to $ZnWO_4$, the FTIR of mixed metal $Zn_{0.5}Co_{0.5}WO_4$ showed the difference in peak shapes and intensities due to the partial replacement of Zn^{2+} ions by Co^{2+} ions [25].

The formation of $ZnWO_4$, $CoWO_4$, and $Zn_{0.5}Co_{0.5}WO_4$ was confirmed by the XRD analysis. Figure 2 shows the XRD pattern of the $ZnWO_4$, $CoWO_4$, and $Zn_{0.5}Co_{0.5}WO_4$ prepared by the hydrothermal method at 180°C for 24 h. The XRD spectra of $ZnWO_4$ shows characteristic peaks at 2θ value of 15.58°, 19.04°, 23.94°, 24.66°, 30.59°, 31.38°, 36.54°, 38.47°, 41.41°, 44.40°, 46.55°, 50.39 51.84°, 53.76°, 54.11°, 61.85°, 64.90°, and 68.34°, which belong to miller indices (010), (100), (011), (110), (111), (020), (021), (200), (121), (112), (211), (220) (130), (221), (202), (113), (132), and (041), respectively (JCPDs card no. 96-210-1675). Then,

the XRD spectra of $CoWO_4$ shows characteristic peaks at 2θ value of 19.02°, 23.88°, 27.72°, 31.50°, 36.44°, 38.69°, 48.52°, 52.17°, 61.89°, and 65.14°, which belong to miller indices (100), (011), (110), (020), (002), (200), (022), (031), (310), and (040), respectively (JCPDs card no. 96-591-0317). Finally, the XRD pattern of $Zn_{0.5}Co_{0.5}WO_4$ NPs shows peaks ascribed to the $ZnWO_4$ at 15.54° (010), 36.41° (021), 41.35° (211), 51.95° (220), 53.94° (130), and 68.56° (041), and peaks ascribed to the $CoWO_4$ at 48.81° (022), 61.81° (310), and 64.96° (040), respectively, which suggests that Co has been successfully doped in the solid matrix of $ZnWO_4$. Moreover, the peak intensities of $Zn_{0.5}Co_{0.5}WO_4$ NPs are greater than pristine $ZnWO_4$ suggesting the increase in crystallinity of the complex upon being mixed with Co^{2+}, which has been proved by data given in Table 1. There are several extra peaks observed in the XRD spectra of $Zn_{0.5}Co_{0.5}WO_4$ which do not belong to either $ZnWO_4$ or $CoWO_4$. These peaks are due to the formation of $Na_2W_2O_7$ and $Na_2W_4O_{13}$ phases with the $Zn_{0.5}Co_{0.5}WO_4$ phase [26,27].

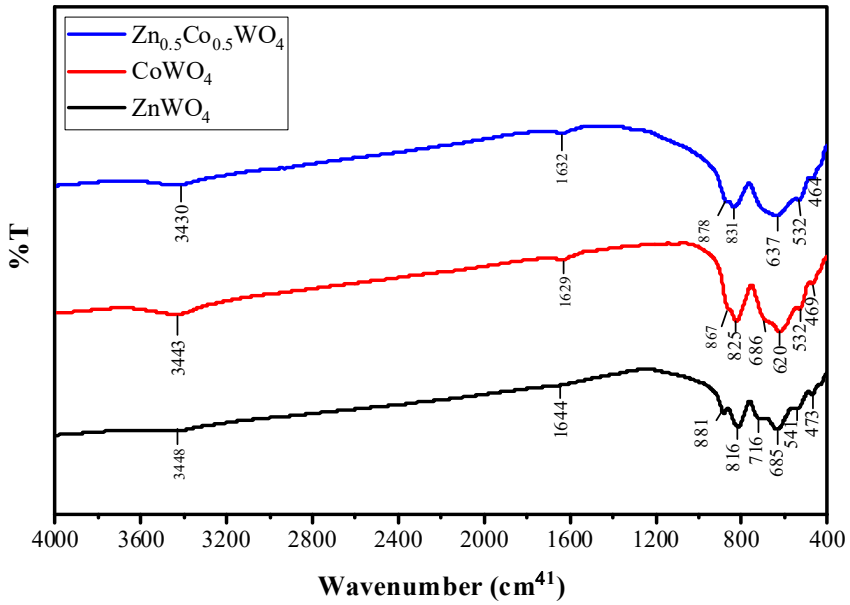


Figure 1. FTIR spectra of $ZnWO_4$ (black line), $CoWO_4$ (purple line), and $Zn_{0.5}Co_{0.5}WO_4$ (light blue line).

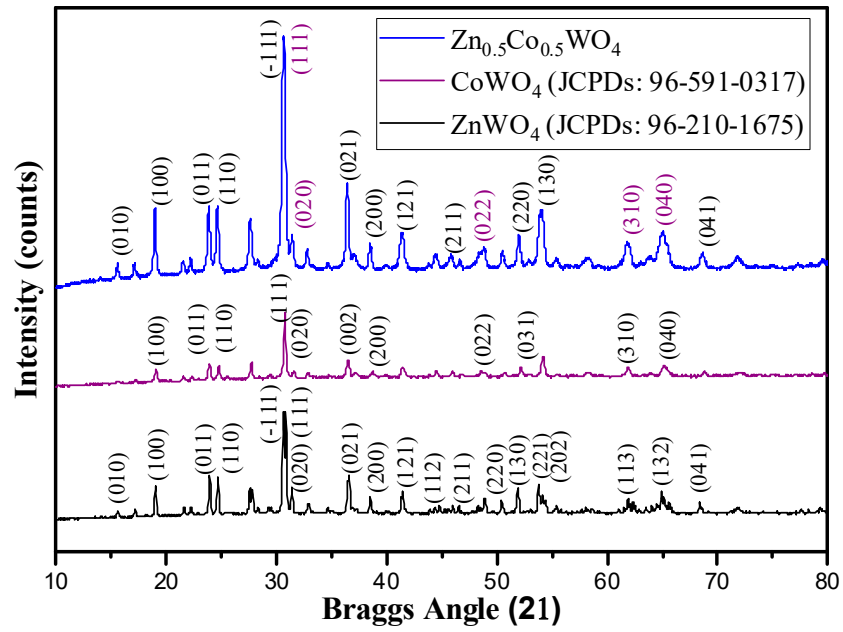


Figure 2. X-ray diffraction pattern of $ZnWO_4$, $CoWO_4$, and $Zn_{0.5}Co_{0.5}WO_4$ calcined at 600 °C.

Table 1. XRD parameter of $ZnWO_4$, $CoWO_4$, and Zn0.5Co0.5WO_4.

Crystallinity (%)	Dislocation Density (δ) Lines ($10^{14} \times m^2$)	Crystallite Size (nm) at 2θ value	Interlayer Spacing (nm) at 2θ	FWHM (β_{hkl})	2θ	Component
45.24	9.78	31.98	0.203	0.45	30.72	$ZnWO_4$
48.46	9.65	32.19	0.195	0.81	30.05	$CoWO_4$
42.18	17.02	24.24	0.198	0.76	30.33	$Zn_{0.5}Co_{0.5}WO_4$

Further information about crystallite size and dislocation density; Scherrer's equation was taken into consideration [28].

$$D = \frac{0.9\lambda}{\beta \cos\theta} \quad (1)$$

$$\text{Dislocation Density}(\delta) = \frac{1}{D^2} \quad (2)$$

$$\text{Interlayer Spacing}(d_{111}) = \frac{n\lambda}{2\text{Sin}\theta} \quad (3)$$

$$\%\text{Crystallinity} = \frac{\text{Area under the crystalline peaks}}{\text{Total area}} \times 100 \quad (4)$$

where D is the crystallite size, λ is the characteristic wavelength of the X-ray, β represents the angular width in radian at an intensity equal to half of its maximum (HWMI) of the peak, and θ is the diffraction angle. Using Equation (1), the average particle size of $ZnWO_4$, $CoWO_4$, and $Zn_{0.5}Co_{0.5}WO_4$ was 31.98, 32.19, and 24.24 nm suggesting a contraction in particle size upon Co inclusion in the $ZnWO_4$ solid lattice.

The surface morphology of the $ZnWO_4$, $CoWO_4$, and $Zn_{0.5}Co_{0.5}WO_4$ were studied using SEM analysis given in (Figure 3). $ZnWO_4$ reveals an aggregation of irregularly shaped crystals with plenty of nanorods (Figure 3a). $CoWO_4$ exhibit uniform nanoparticles of various size (Figure 3b), while $Zn_{0.5}Co_{0.5}WO_4$ revealed an assembly of fine nanoparticles with a porous surface (Figure 3c). The elemental composition of the synthesized $Zn_{0.5}Co_{0.5}WO_4$ NPs was observed by EDX analysis and the results showed the presence of the element (weight%) as O (28.52%), Zn (4.55%), Co (4.22%), and W (62.81%), which confirms the successful deposition of Co^{2+} in the $ZnWO_4$ lattice (Figure 3d). The high atomic percentage of W in the EDX spectra is due to the presence of impurity in the form of $Na_2W_2O_7$ and $Na_2W_4O_{13}$ phases with the $Zn_{0.5}Co_{0.5}WO_4$, which resulted in an extra amount of W in the EDX spectra [27].

Furthermore, to figure out the size of the $ZnWO_4$, $CoWO_4$, and $Zn_{0.5}Co_{0.5}WO_4$, TEM analysis was performed (Figure 4a–c). $ZnWO_4$ (Figure 4a) is composed of particles with a rod-like shape; $CoWO_4$ (Figure 4b) presented a morphologically spherical shaped particle. The synthesized material $Zn_{0.5}Co_{0.5}WO_4$ (Figure 4c) exhibited particles mixed of nanorods with some spherical particles with size in a range from 5 to 60 nm, and the Gaussian distribution of the average size was found to be 31 nm given in Figure 4d. Figure 4e represents the TEM image of $Zn_{0.5}Co_{0.5}WO_4$, which suggested the shape of particles to be distorted monoclinic due to the doping of Co into the $ZnWO_4$ lattice. Selected area electron diffraction (SAED) analysis (Figure 4f) was further considered to simulate the TEM data with XRD to assess the purity and shape of the nanoparticles. It contains patterns originating from diffraction points in the TEM screen belonging to randomly oriented nanoparticles. The occurrence of diffraction patterns in Figure 4f suggested that the material is crystalline and pure. The hkl values belonging to yellow fringes simulate the XRD hkl planes of $Zn_{0.5}Co_{0.5}WO_4$ suggesting the shape of the nanoparticles to be monoclinic.

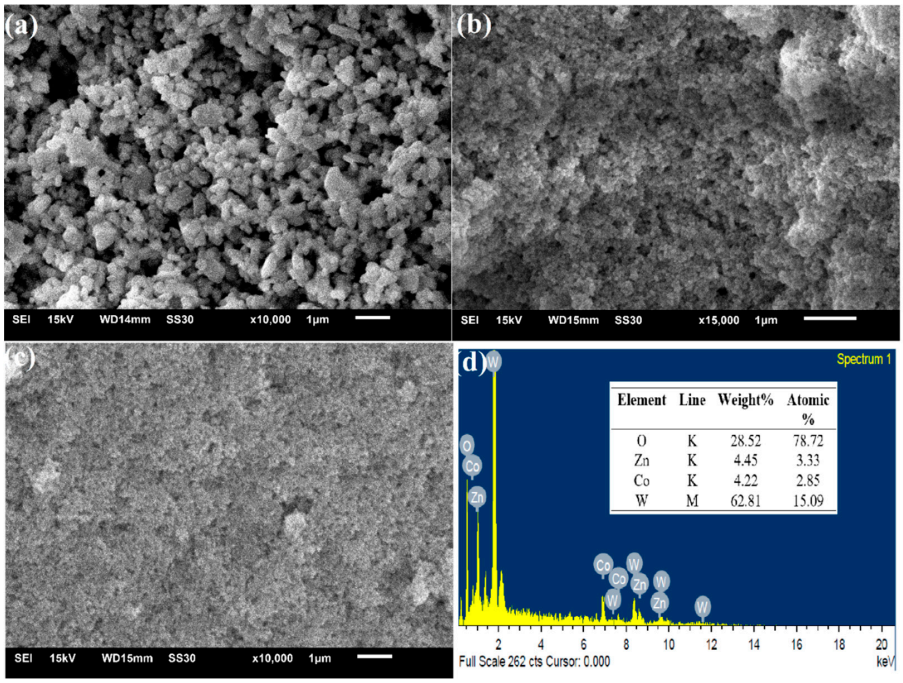


Figure 3. SEM micrographs of (**a**) $ZnWO_4$ NPs; (**b**) $CoWO_4$ NPs; (**c**) $Zn_{0.5}Co_{0.5}WO_4$ at 1 μm scale; (**d**) EDX spectra of $Zn_{0.5}Co_{0.5}WO_4$ in 0–20 keV range.

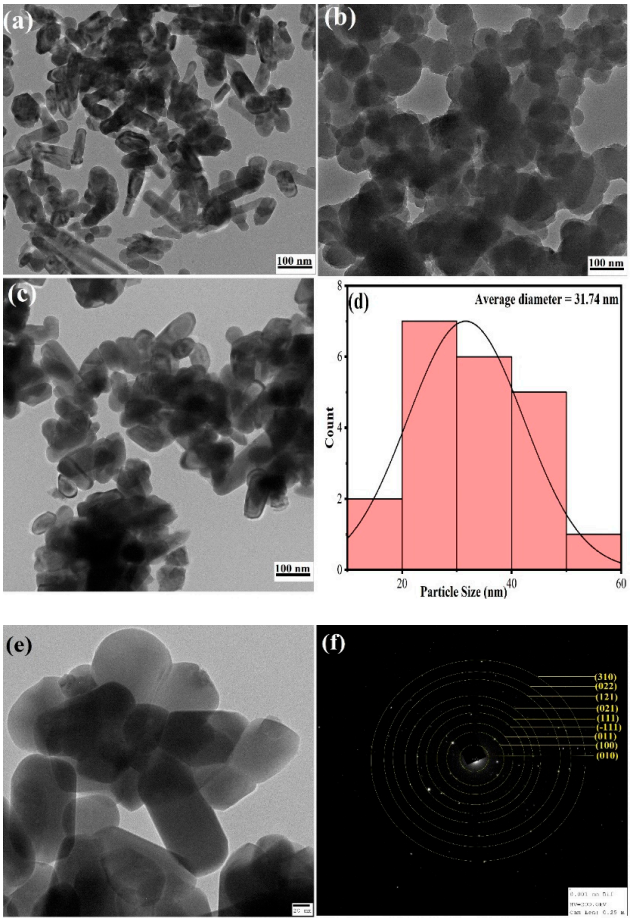


Figure 4. TEM images of (**a**) $ZnWO_4$; (**b**) $CoWO_4$; (**c**) $Zn_{0.5}Co_{0.5}WO_4$ at 100 nm magnification range; (**d**) particle size histogram; (**e**) TEM image of $Zn_{0.5}Co_{0.5}WO_4$ at 20 nm magnification range; (**f**) selected area electron diffraction (SAED) image of $Zn_{0.5}Co_{0.5}WO_4$.

The optical properties of the synthesized NPs and their energy bandgap were estimated by using UV–vis spectroscopy in the range of 200–700 nm and the results are given in Figure 5. The absorption spectra of all the synthesized NPs $ZnWO_4$, $CoWO_4$, and $Zn_{0.5}Co_{0.5}WO_4$ exhibited two peaks, one around 260–312 nm and another broad peak around 530–650 nm, suggesting the UV–vis activeness of the NPs. The inset in Figure 5 shows Tauc's plot, which is used to calculate band gap energy (Eg) of the prepared samples by using the Equation (5) [29];

$$(\alpha h\nu) = A(h\nu - E_g)^n \quad (5)$$

where α is the absorption coefficient, A is constant, h is plank constant, ν is the frequency of radiations, and n is a constant of transition variations, i.e., n = 1/2 for direct transitions and n = 2 for the indirect transitions. Tauc's plot indicated that the synthesized $ZnWO_4$, $CoWO_4$, and $Zn_{0.5}Co_{0.5}WO_4$ were found to have an energy bandgap value of 3.49 eV, 3.42 eV, and 3.33 eV, respectively. Results showed that the deposition of Co^{2+} in the $ZnWO_4$ solid lattice results in the increase in absorption edge by decreasing the energy bandgap, which inhibits the rate of electron–hole pair recombination, and thus improves the photocatalytic efficiency of the synthesized material [30]. The doping of Co^{2+} into $ZnWO_4$ leads to the induction of deformations in the pure monoclinic lattice of $ZnWO_4$, which creates mobile oxygen vacancies in the cluster and makes an improvement in the catalytic [31,32].

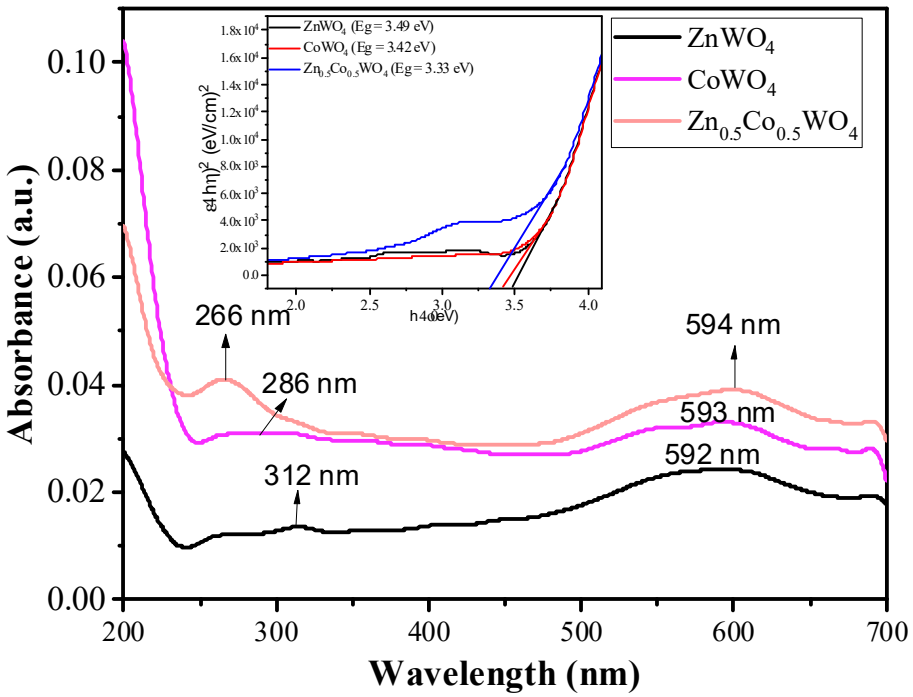


Figure 5. UV–vis plot of $ZnWO_4$ NPs, $CoWO_4$, and $Zn_{0.5}Co_{0.5}WO_4$ in the wavelength range of 200–700 nm (inset is the Tauc's plot for calculating the band gap energy (E_g) of the material).

Figure 6 consists of the photoluminescence emission spectra of $ZnWO_4$, $CoWO_4$, and $Zn_{0.5}Co_{0.5}WO_4$ recorded at a 594 nm excitation wavelength. It can be seen that the PL spectra spans in the range of 545 to 575 nm with a prominent emission peak at 558 nm. The information obtained from the PL spectra suggested that the PL intensity of synthesized $Zn_{0.5}Co_{0.5}WO_4$ was found to be lower than that of $ZnWO_4$ and $CoWO_4$. The inclusion of Co in the wolframite monoclinic structure of $ZnWO_4$ results in emissions due to the radiative transition between W and O in the WO_6^{6-} molecular complex, which effectively slows down the electron–hole [33–35].

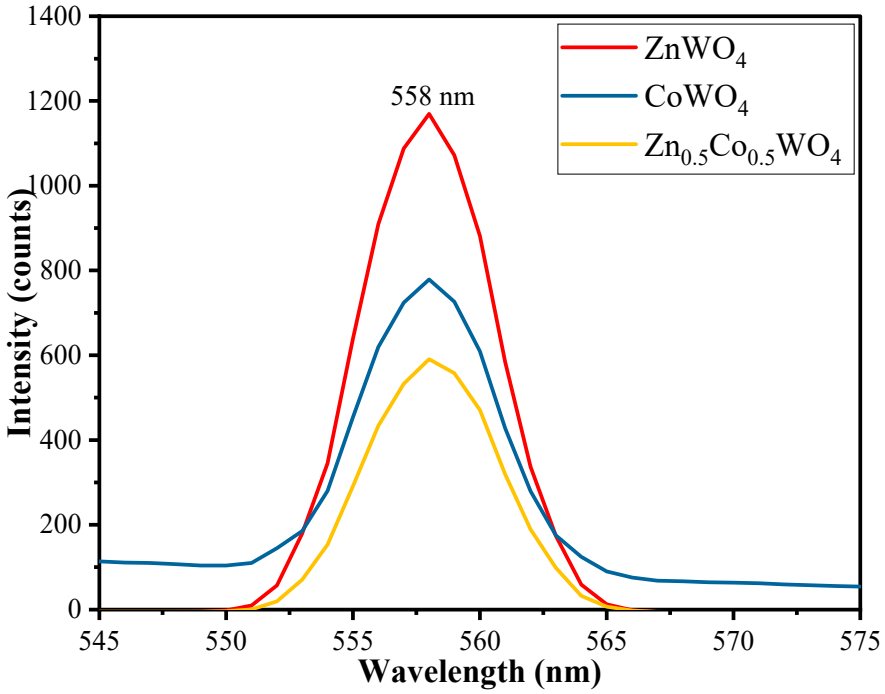


Figure 6. Photoluminescence (PL) spectra of $ZnWO_4$, $CoWO_4$ and $Zn_{0.5}Co_{0.5}WO_4$ were recorded at a 594 nm excitation wavelength dispersed in methanol.

2.2. Photocatalytic Experiments and Optimization of Reaction Parameters

2.2.1. Effect of Variable XO Concentration

The concentration of the dye solution is an important parameter for elucidating the photocatalytic efficiency of the material. Photocatalytic experiments were conducted by taking 10 mg of NPs as a catalyst with variable (20–100 ppm) XO concentration for 120 min of visible light irradiation. The results obtained are given in Figure 7a–d, which suggest that $Zn_{0.5}Co_{0.5}WO_4$ possesses better photocatalytic efficiency (97.17%) as compared to $CoWO_4$ (91.81%), followed by $ZnWO_4$ (89.51%) for 60 ppm of XO, but as the concentration of XO increases beyond 60 ppm, the percentage degradation decreases (Figure 7d). The causes could include: (1) XO may cover more $ZnWO_4$, $CoWO_4$, and $Zn_{0.5}Co_{0.5}WO_4$ active sites, which inhibits the production of oxidants ($^{\bullet}OH$ or $^{\bullet}O_2^-$ radicals) and lowers the efficiency of degradation: and (2) higher XO concentration absorbs a greater number of photons, and as a result, there are not enough photons to activate the surfaces of $ZnWO_4$, $CoWO_4$, and $Zn_{0.5}Co_{0.5}WO_4$ nanoparticles, which slows down XO's degradation at higher concentrations [36]. So, 60 ppm XO concentration was chosen as the optimum concentration for further photocatalytic experiments.

2.2.2. Effect of Variable Catalyst Dose

The physicochemical characteristics of nanomaterials, such as surface area, phase structure, particle size, and interface charge, make them able to complete adsorption action [27]. To efficiently degrade XO through catalysis using the catalyst, the photocatalytic experiment was performed by varying catalyst doses, such as 5, 10, 15, and 20 mg with 10 mL of 10 ppm XO. The results given in Figure 8a–d suggested that the photocatalytic efficiency increased from 5 mg catalyst dose to 10 mg and starts declining with further increase. All the synthesized NPs exhibit maximum photocatalytic efficiency at 10 mg catalyst dose as 97.89% for $ZnWO_4$, 98.10% for $CoWO_4$, and 98.77% for $Zn_{0.5}Co_{0.5}WO_4$. More active sites are produced on the catalyst's surface at lower concentrations, which promotes the creation of $^{\bullet}OH$ or $^{\bullet}O_2^-$ radicals. After that, increasing the catalytic dose causes the particles to agglomerate and sediment, which increases the turbidity and opacity of the slurry. Hence,

the generation of $^{\bullet}OH$ or $^{\bullet}O_2^-$ radicals automatically decrease [24]. Therefore, the catalyst dose of 10 mg was chosen to be the optimum dose for the degradation.

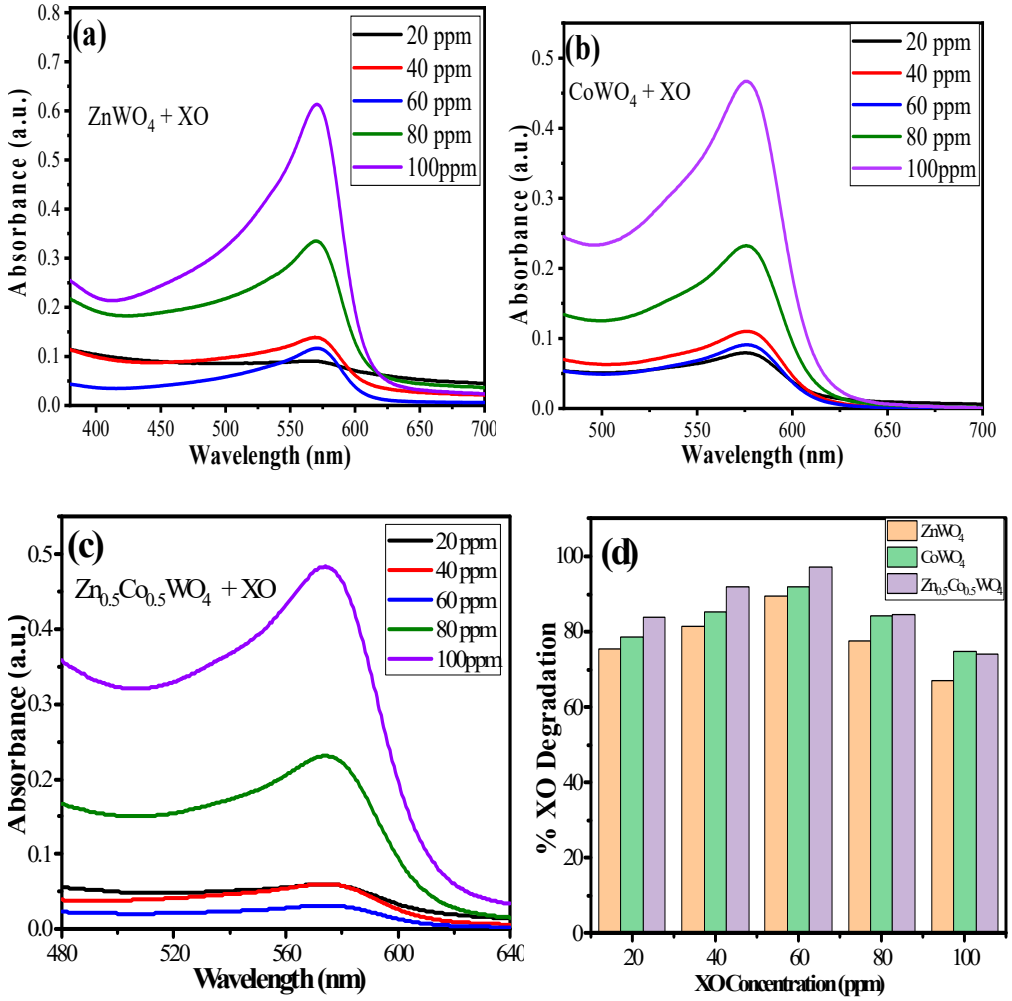


Figure 7. Effect of initial concentration of XO dye on photocatalytic degradation by (**a**) $ZnWO_4$; (**b**) $CoWO_4$; (**c**) $Zn_{0.5}Co_{0.5}WO_4$; (**d**) XO degradation (%) vs. XO concentration bar graph.

2.2.3. Effect of pH

Experiments were performed to evaluate the impact of pH on the photocatalytic efficiencies of $ZnWO_4$, $CoWO_4$, and $Zn_{0.5}Co_{0.5}WO_4$. A total of 10 mg of the catalyst was dispersed in 20 mL of 60 ppm XO solution with a variable pH range from 1–7, and irradiated for 120 min under the visible light source. The obtained results after the experiments are given in Figure 9, which suggests that the photocatalytic efficiency of all the catalysts increased until pH 3, giving a maximum value of 93.35% for $ZnWO_4$, 96.21% for $CoWO_4$, and 97.97% for $Zn_{0.5}Co_{0.5}WO_4$. Further, an increase in pH value beyond 3 results in a decrease in photocatalytic efficiency with a continuous fall until pH 7. So, pH 3 was taken as the optimum pH value for the photocatalytic experiments. The trend can be explained by the fact that as XO is an anionic dye, it can easily bind with the positive surface of the catalyst at low pH through electrostatic interactions, and thereby, in the presence of light, it gets degraded by $^{\bullet}OH$ or $^{\bullet}O_2^-$ radicals [7]. As the pH values increase, the surface becomes negative, which will exert a repulsive force on the anionic XO molecule, and hence, the photocatalytic efficiency decreases.

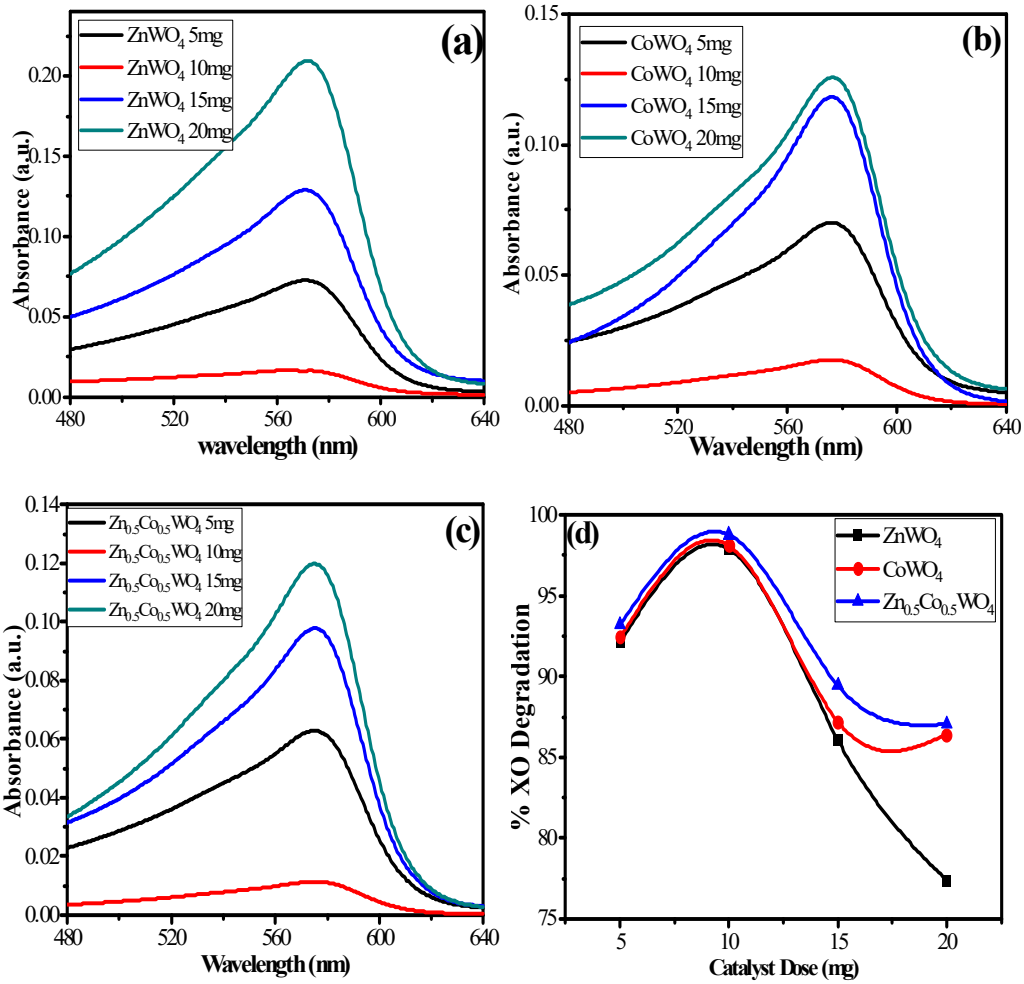


Figure 8. Photocatalytic degradation of XO with a different catalytic dose of (**a**) $ZnWO_4$; (**b**) $CoWO_4$; and (**c**) $Zn_{0.5}Co_{0.5}WO_4$; and (**d**) %degradation vs. catalyst dose graph.

2.3. Kinetics of Photodegradation

A variety of experiments were carried out by taking 10 mL of 20 ppm XO with 10 mg of catalyst at varying irradiation time from 0 to 120 min under visible solar radiation, and the data obtained was adjusted to the Langmuir–Hinshelwood (L–H) pseudo-first-order kinetic model for the quantitative analysis of XO degradation [37,38].

$$-\ln\left(\frac{C_e}{C_o}\right) = k_{app} \times t \quad (6)$$

where C_o represents the initial concentration and C_t represents the final concentration of XO at time t. The results are given in Figure 10a–d, in which it was observed that with an increase in irradiation time, the photocatalytic efficiency increases. This may be due to an increase in irradiation time, the surface of the catalyst becomes more activated by absorbing the solar radiation and generates a greater number of ROS $^{\bullet}OH$ or $^{\bullet}O_2^-$ radicals which interact with dye molecules and degrade them [39]. The slope of the pseudo-first-order reaction (Figure 10d) can be utilized to determine the value of k_{app} from the plot of $-\ln(C_e/C_0)$ vs. time (min), which shows a linear response. The obtained values of k_{app} given in Table 2 as 0.018 min^{-1} for $ZnWO_4$, 0.021 min^{-1} for $CoWO_4$, and 0.025 min^{-1} for $Zn_{0.5}Co_{0.5}WO_4$ proved the high efficiency of $Zn_{0.5}Co_{0.5}WO_4$ as compared to pristine $ZnWO_4$ and $CoWO_4$. The obtained value of $R^2 = 0.99$ for all the nanoparticles suggested that the photocatalytic data can be realistically simulated by the L–H model. The outcomes demonstrate that the deposition of Co^{2+} in $ZnWO_4$ of both catalysts considerably improves

the degrading ability compared to each catalyst individually. Finally, $Zn_{0.5}Co_{0.5}WO_4$was the novel composite having distinctive characteristics when compared to other composites.

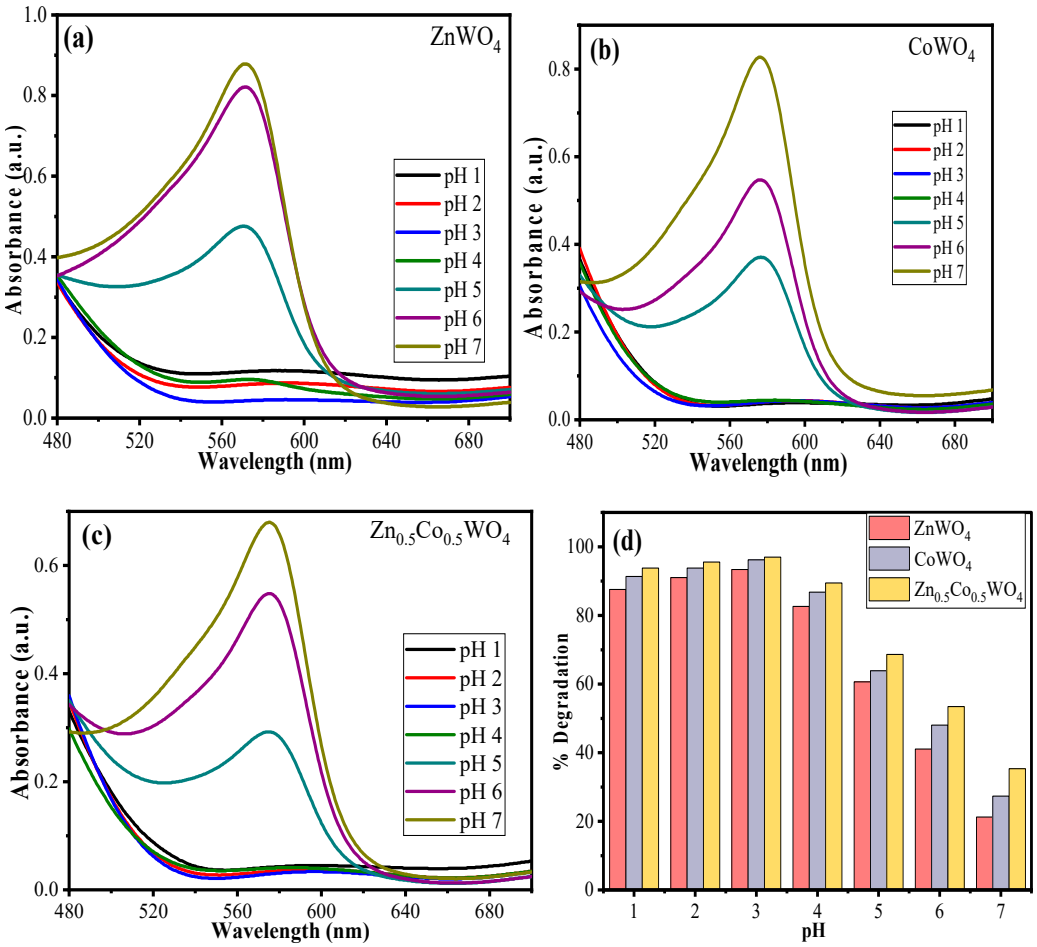


Figure 9. Effect of solution pH on photocatalytic degradation by (**a**) $ZnWO_4$; (**b**) $CoWO_4$; (**c**) $Zn_{0.5}Co_{0.5}WO_4$; (**d**) XO degradation (%) vs. pH bar graph.

Table 2. The kinetic parameters for the degradation of XO dye (20ppm) using 10 mg $ZnWO_4$, $CoWO_4$, and $Zn_{0.5}Co_{0.5}WO_4$ with variable irradiation time (5–120 min).

Material	k_1 (min^{-1})	R^2	$t_{1/2}$ (min)
$ZnWO_4$	0.018	0.99	38.50
$CoWO_4$	0.021	0.99	33.00
$Zn_{0.5}Co_{0.5}WO_4$	0.025	0.99	27.72

2.4. Scavenging Study and Mechanism of Photodegradation

It was suggested that a variety of reactive species, including the hydroxyl radical ($^{\bullet}OH$), superoxide ($^{\bullet}O_2^-$), valence band hole (h^+), and electron (e^-) play important roles in the photodegradation of organic pollutants, and their effectiveness depends upon the band structure and chemical nature of the photocatalysts [40]. So, scavenger studies were performed using a 1.3 mM solution of Benzoic acid (BA), Potassium dichromate ($K_2Cr_2O_7$), (AA), ethylenediaminetetraacetic acid (EDTA), and benzoquinone (BQ) by taking 10 mL of 20ppm XO with 10 mg at pH 3 for an irradiation time of 120 min. We know that BA is a scavenger for $^{\bullet}OH$, EDTA for h^+, $K_2Cr_2O_7$ for e^-, and BQ for $^{\bullet}O_2^-$ [41,42]. Figure 11 displays the results, which show that without the use of a scavenger, the degrading efficiency of $Zn_{0.5}Co_{0.5}WO_4$ towards XO achieved 98.27%. After adding BA and EDTA, there appears no appreciable change in photocatalytic efficiency, suggesting no primary role of $^{\bullet}OH$

and h^+ on the degradation of XO at the optimized conditions. On the contrary, when BQ and $K_2Cr_2O_7$ are added, an appreciable decrease in photocatalytic efficiency happens, demonstrating that photogenerated electrons (e^-) and $^{\bullet}O_2^-$ radicals are predominant species in this photodegradation reaction scheme. The results showed that the degradation of XO was primarily controlled by e^- and $^{\bullet}O_2^-$ radicals (majorly).

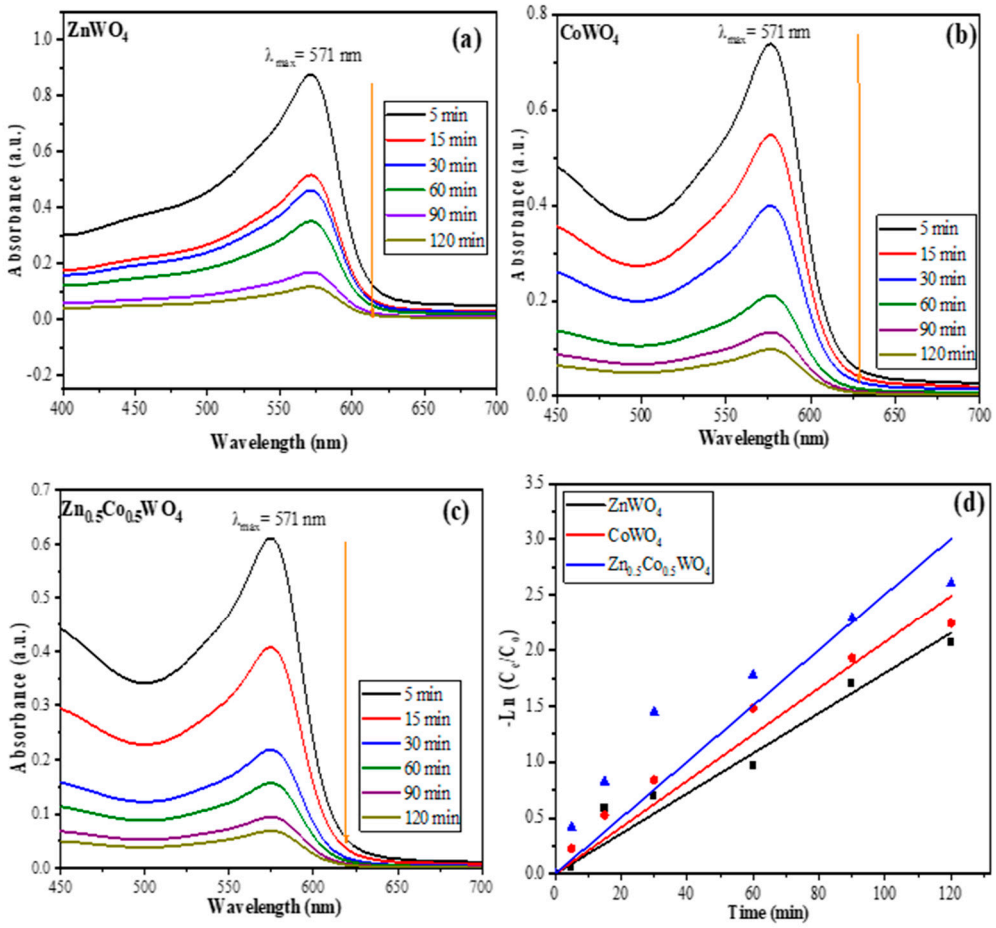


Figure 10. UV–vis absorption spectra of degraded XO dye (60 ppm) using 10 mg of (**a**) $ZnWO_4$; (**b**) $CoWO_4$; (**c**) $Zn_{0.5}Co_{0.5}WO_4$; and (**d**) L–H model pseudo-first-order kinetic graph with variable irradiation time (5–120 min).

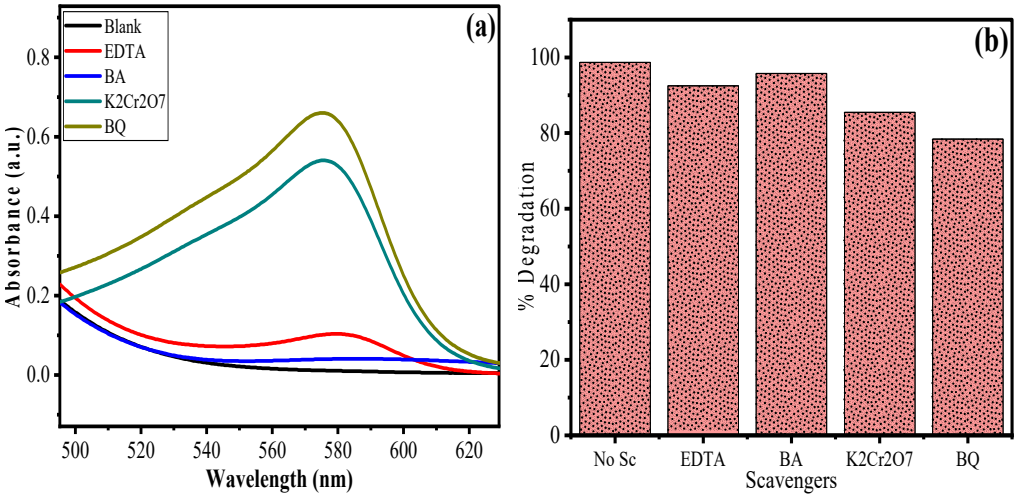


Figure 11. (**a**) UV–vis spectra of XO degradation in the presence of various scavengers; (**b**) % XO degradation vs. bar graph associated with each scavenger.

The plausible mechanism of degradation of XO by $^{\bullet}O_2^-$ radicals is given in Figure 12 [43,44].

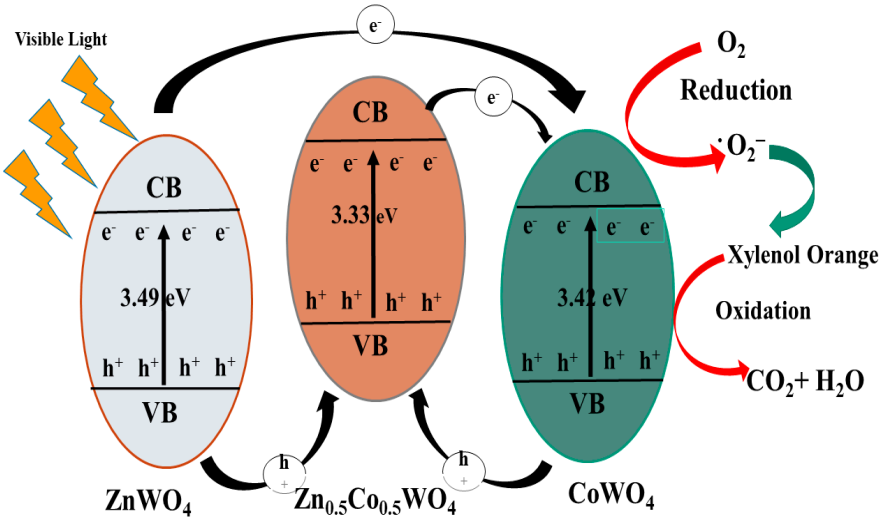


Figure 12. A plausible mechanism of degradation of XO by synthesized $Zn_{0.5}Co_{0.5}WO_4$.

2.5. Comparison with the Literature

The outcomes of this study were compared with the information available in the literature, and a comparison in Table 3 was made to investigate the upgraded scientific information added by the present study. It was found that there is no research where tungstate base nanomaterial is used for the photocatalytic degradation of xylenol orange.

Table 3. Comparison of the literature information with the present study.

Catalysts	Irradiation Time (min)	Light Source	Dye Used	% Degradation	References
$BiOBr/ZnWO_4$	170	UV-A light	RhB	99.40	[45]
La: $ZnWO_4$	90	UV light	MB	97.00	[46]
$CoWO4/ZnWO_4$ p-n heterojunction	40	Xe lamp	RhB	93%	[47]
$ZnWO4/WO_3$ heterojunction	120	Visible light	MB	83.60	[48]
ZnWO4-(ZnO)	120	UV-illumination	MO	99.00	[49]
CDs-$ZnWO_4$	150	UV-illumination	NGB	93.00	[50]
$Zn_{0.5}Co_{0.5}WO_4$	120	Visible Solar Light	XO	98.77	Present Study

2.6. Reusability Test

The reusability test was performed for the synthesized $Zn_{0.5}Co_{0.5}WO_4$ up to five cycles to assess the stability of the material towards XO degradation, and the results are given in Figure 13a. It can be seen that there is no appreciable change in photocatalytic efficiency up to the first two cycles with greater than 98% of XO degradation. Furthermore, from cycle 3 to cycle 5, there appears some appreciable decrease in photocatalytic efficiency attaining 85% of XO degradation in cycle 5. The overall results suggest that the synthesized $Zn_{0.5}Co_{0.5}WO_4$ have good stability toward the XO degradation under optimized reaction conditions. To support the stability of the material, XRD analysis of the synthesized material before and after the photocatalytic reaction was taken into consideration, which is given in Figure 13b. The XRD spectra of $Zn_{0.5}Co_{0.5}WO_4$ after five consecutive cycles of reuse represented almost similar hkl planes, but with reduced intensity as compared to pristine $Zn_{0.5}Co_{0.5}WO_4$ before the photocatalytic reaction. Only one change was observed, that after the photocatalytic reaction the (-111) plane diminished, which may be due to the absorption of water.

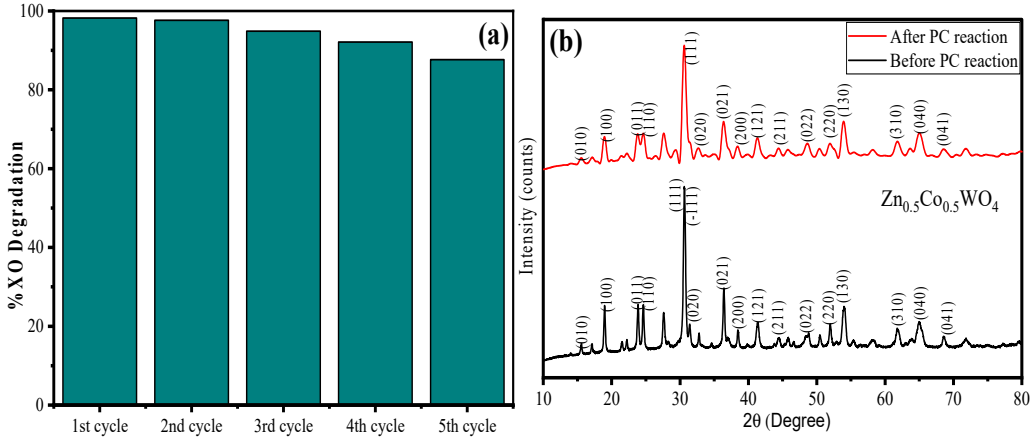


Figure 13. (**a**) Reusability test for synthesized $Zn_{0.5}Co_{0.5}WO_4$ NPs for XO degradation (**b**) XRD spectra of $Zn_{0.5}Co_{0.5}WO_4$ before and after the photocatalytic (PC) reaction.

3. Materials and Methods

3.1. Chemicals and Reagents

Sodium tungstate dihydrate ($Na_2WO_4{\cdot}2H_2O$, ACS grade, 99%) was purchased from Merck, Rahway, NJ, USA. Cobalt (II) nitrate hexahydrate (Co $(NO_3)_2.6H_2O$ ACS grade 98%), Zinc nitrate hexahydrate (Zn $(NO_3)_2.6H_2O$, reagent grade 98%), were purchased from Sigma Aldrich, St. Louis, Missouri USA. Xylenol orange ($C_{31}H_{28}N_2Na_4O_{13}S$, GR) and Ammonia solution (25%) were acquired from Otto Chemie, Mumbai, India. All the solutions were prepared in deionized (DI) water and used throughout all the photocatalytic experiments. Figure 14 represents the molecular structure of xylenol orange.

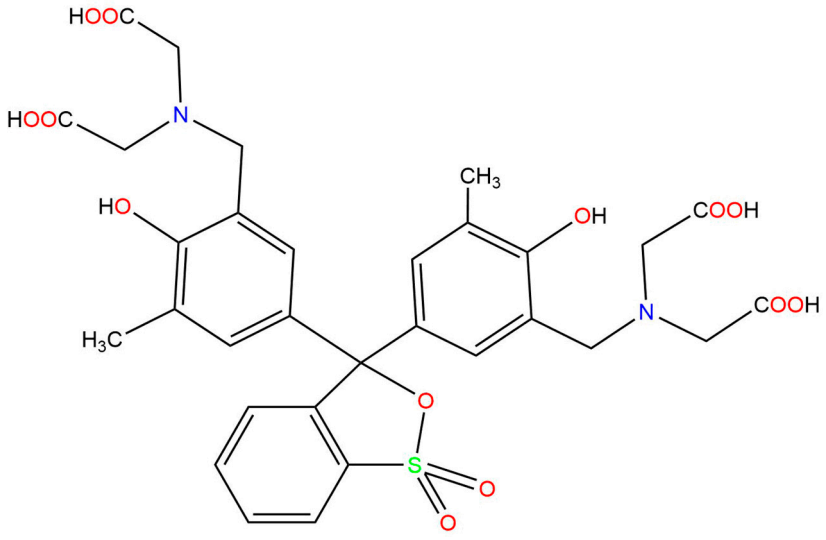


Figure 14. Structure of xylenol orange (XO).

3.2. Synthesis of $ZnWO_4$, $CoWO_4$, and $Zn_{0.5}Co_{0.5}WO_4$ Nanoparticles

The synthesis of pristine metal tungstate nanomaterials ($ZnWO_4$, $CoWO_4$ NPs) and mixed metal tungstate nanocomposite ($Zn_{0.5}Co_{0.5}WO_4$) was done according to the hydrothermal method reported elsewhere [51]. Three Erlenmeyer flasks of 50 mL capacity were equipped with 25 mL of 3mmol of sodium tungstate dihydrate ($Na_2WO_4{\cdot}2H_2O$), Zinc nitrate hexahydrate ($Zn(NO_3)_2{\cdot}6H_2O$; Flask 1), Cobalt(II)nitrate hexahydrate (Co $(NO_3)_2{\cdot}6H_2O$; Flask 2), and 1:1 ratio, i.e., 1.5 mmol each, of $Zn(NO_3)_2{\cdot}6H_2O$ and Co $(NO_3)_2{\cdot}6H_2O$ (Flask 3). All the flasks were placed on a magnetic stirring plate for 30 min to completely dissolve the salts and attain homogeneity. Then, the mixtures (F1, F2, and F3) were transferred into a Teflon-lined steel autoclave and heated in a convection oven at

180 °C for 24 h. The resulting precipitates of $ZnWO_4$, $CoWO_4$, and $Zn_{0.5}Co_{0.5}WO_4$ were centrifuged at 8000 rpm for 5 min and purified several times with DI water and finally with ethanol (2 times). After that, the materials were dried at 100 °C for 5 h and calcined at 600 °C for 4 h, then stored in a desiccator using a polystyrene Petri dish for further characterization and photocatalytic experiments.

3.3. Characterization Techniques

The $ZnWO_4$, $CoWO_4$, and $Zn_{0.5}Co_{0.5}WO_4$ were characterized using various techniques. The change in crystallite size and interplanar distance on Co deposition in the crystal lattice of $ZnWO_4$ was analyzed by an X-ray powder diffractometer (XRD, Rigaku Ultima IV, Tokyo, Japan) at Cu Kα wavelength of 1.5418 Å as a source of radiation. The change of WO_6^{6-} octahedron vibrations, Zn–O, and formation of Co–O bonding was assessed through Fourier transform infrared (FTIR) spectroscopy using a Perkin Elmer Spectrum 2 ATR spectrometer (Perkin Elmer, Waltham, MA, USA). The optical properties, energy bandgap of the synthesized NPs, and remaining concentration of XO in the effluent after the photocatalytic experiment was calculated by using a Shimadzu UV–1900 double-beam spectrophotometer (Kyoto, Japan). The surface morphology of the synthesized NPs was observed by scanning electron microscopy (SEM; JEOL GSM 6510LV, Tokyo, Japan) associated with an X-ray energy dispersive detector (EDX) to investigate the elemental composition and mapping. The morphological change in shape and size of the nanocrystalline solid upon Co deposition in $ZnWO_4$ was investigated using a transmission electron microscope (TEM; JEM 2100, Tokyo, Japan).

3.4. Photocatalysis Experiment

The photocatalytic efficiency of $ZnWO_4$, $CoWO_4$, and $Zn_{0.5}Co_{0.5}WO_4$ was analyzed towards the degradation of xylenol orange under visible light irradiation in a photocatalytic reactor. An aliquot of 10 mL of 50 ppm XO was taken in a 20 mL 1.8 cm glass tube with a magnetic bar of 10 mg of synthesized NPs in a photocatalytic reactor using Xe lamp (420 W cm $^{-1}$) for 5–120 min of irradiation. The aliquots are taken out of the photoreactor at a regular time interval, centrifuged to separate the nanocatalyst, and then placed in a UV–vis spectrophotometer at λ_{max} = 580 nm to check the photocatalytic efficiency of the synthesized NPs, which is given by Equation (7);

$$\text{XO Degradation}(\%) = \left(\frac{C_0 - C_e}{C_0}\right) \times 100 \quad (7)$$

where C_0 and Ce represents the initial concentration of an organic pollutant at time t = 0 and at any time t, respectively. The experiments were repeated by changing the parameters, for instance, organic pollutant concentration (ppm), irradiation time (min), catalytic load (mg), and pH of the media to optimize the reaction condition and predict the mechanism of the degradation.

4. Conclusions

The present study reveals the hydrothermal synthesis of pristine $ZnWO_4$, $CoWO_4$, and mixed metal $Zn_{0.5}Co_{0.5}WO_4$ nanoparticles (NPs) in a Teflon-lined autoclave at 180 °C for 24 h. The structural, morphological, elemental, and optical analyses supported the formation of $Zn_{0.5}Co_{0.5}WO_4$. The XRD analysis revealed a contraction in crystallite size from 32 nm to 24 nm with a decrease in crystallinity from 45% to 42% in $ZnWO_4$ to $Zn_{0.5}Co_{0.5}WO_4$ suggesting the successful deposition of Co^{2+} in the $ZnWO_4$ lattice. The TEM analysis suggested the nanorod-like shape of the $Zn_{0.5}Co_{0.5}WO_4$ NPs with an average particle size of 31.74 nm. The optical studies revealed the UV–vis light activeness of materials with the energy band gap of $ZnWO_4$ (3.49 eV), $CoWO_4$ (3.42 eV), and mixed metal $Zn_{0.5}Co_{0.5}WO_4$ (3.33 eV). The material was explored as a catalyst for the photodegradation of XO dye under visible solar radiation and the results suggested the order of photocatalytic efficiency as $Zn_{0.5}Co_{0.5}WO_4$ (98.77%) > $CoWO_4$ (98.10%) > $ZnWO_4$ (97.89%) utilizing 10 mg

of catalyst for 60 ppm XO for 120 min of solar irradiation. The photocatalytic data were well explained by L–H pseudo–first–order kinetics with R^2 = 0.99, and apparent rate constant (k_{app}) as 0.018 min^{-1} for $ZnWO_4$, 0.021 min^{-1} for $CoWO_4$, and 0.025 min^{-1} for $Zn_{0.5}Co_{0.5}WO_4$. The scavenger experiments disclosed that superoxide anion radicals ($\bullet O_2^-$) and photogenerated electrons (e^-) played important roles in the degradation of XO. The outcomes of this study revealed that the eco-friendly and economical hydrothermal synthesized material (Zn0.5Co0.5WO4) can be used more efficiently for the treatment of XO-contaminated water in industries without the generation of any secondary pollution.

Author Contributions: Conceptualization, F.A.A.; Methodology, F.A.A., H.S.A. and I.H.; Software, I.H.; Validation I.H.; Investigation, W.S.A.-N. and A.A.A.; Resources, W.S.A.-N. and A.A.A.; Data curation, I.H.; Writing—original draft, W.S.A.-N.; Writing—review & editing, H.S.A. and I.H.; Visualization, I.H.; Supervision, F.A.A. and H.S.A.; Project administration, F.A.A.; Funding acquisition, F.A.A. All authors have read and agreed to the published version of the manuscript.

Funding: The authors extend their appreciation to the Deputyship of Research and Innovation, Ministry of Education in Saudi Arabia for funding this research work through project number (IFKSURG-2-255).

Conflicts of Interest: The authors declare no conflict of interest.

References

1. You, J.; Wang, L.; Zhao, Y.; Bao, W. A Review of Amino-Functionalized Magnetic Nanoparticles for Water Treatment: Features and Prospects. *J. Clean. Prod.* **2021**, *281*, 124668. [CrossRef]
2. Surendra, B.S.; Shashi Shekhar, T.R.; Veerabhadraswamy, M.; Nagaswarupa, H.P.; Prashantha, S.C.; Geethanjali, G.C.; Likitha, C. Probe Sonication Synthesis of $ZnFe_2O_4$ NPs for the Photocatalytic Degradation of Dyes and Effect of Treated Wastewater on Growth of Plants. *Chem. Phys. Lett.* **2020**, *745*, 137286. [CrossRef]
3. Akbari, A.; Sabouri, Z.; Hosseini, H.A.; Hashemzadeh, A.; Khatami, M.; Darroudi, M. Effect of Nickel Oxide Nanoparticles as a Photocatalyst in Dyes Degradation and Evaluation of Effective Parameters in Their Removal from Aqueous Environments. *Inorg. Chem. Commun.* **2020**, *115*, 107867. [CrossRef]
4. Sarkar, S.; Ponce, N.T.; Banerjee, A.; Bandopadhyay, R.; Rajendran, S.; Lichtfouse, E. Green Polymeric Nanomaterials for the Photocatalytic Degradation of Dyes: A Review. *Environ. Chem. Lett.* **2020**, *18*, 1569–1580. [CrossRef] [PubMed]
5. Xu, P.P.; Zhang, L.; Jia, X.; Wang, X.; Cao, Y.; Zhang, Y. Visible-Light-Enhanced Photocatalytic Activities for Degradation of Organics by Chromium Acetylacetone Supported on UiO-66-NH2. *ChemistrySelect* **2020**, *5*, 14877–14883. [CrossRef]
6. Garg, N.; Bera, S.; Rastogi, L.; Ballal, A.; Balaramakrishna, M.V. Synthesis and Characterization of L-Asparagine Stabilised Gold Nanoparticles: Catalyst for Degradation of Organic Dyes. *Spectrochim. Acta Part A Mol. Biomol. Spectrosc.* **2020**, *232*, 118126. [CrossRef]
7. Kumar, O.P.; Shahzad, K.; Nazir, M.A.; Farooq, N.; Malik, M.; Ahmad Shah, S.S.; ur Rehman, A. Photo-Fenton Activated C3N4x/AgOy@Co1-XBi0.1-YO7 Dual s-Scheme Heterojunction towards Degradation of Organic Pollutants. *Opt. Mater.* **2022**, *126*, 112199. [CrossRef]
8. Jamshaid, M.; Nazir, M.A.; Najam, T.; Shah, S.S.A.; Khan, H.M.; ur Rehman, A. Facile Synthesis of Yb^{3+}-Zn^{2+} Substituted M Type Hexaferrites: Structural, Electric and Photocatalytic Properties under Visible Light for Methylene Blue Removal. *Chem. Phys. Lett.* **2022**, *805*, 139939. [CrossRef]
9. Shahzad, K.; Hussain, S.; Nazir, M.A.; Jamshaid, M.; ur Rehman, A.; Alkorbi, A.S.; Alsaiari, R.; Alhemiary, N.A. Versatile Ag_2O and ZnO Nanomaterials Fabricated via Annealed Ag-PMOS and ZnO-PMOS: An Efficient Photocatalysis Tool for Azo Dyes. *J. Mol. Liq.* **2022**, *356*, 119036. [CrossRef]
10. Xu, L.; Wang, X.; Xu, M.L.; Liu, B.; Wang, X.F.; Wang, S.H.; Sun, T. Preparation of Zinc Tungstate Nanomaterial and Its Sonocatalytic Degradation of Meloxicam as a Novel Sonocatalyst in Aqueous Solution. *Ultrason. Sonochem.* **2020**, *61*, 104815. [CrossRef]
11. Taneja, P.; Sharma, S.; Umar, A.; Mehta, S.K.; Ibhadon, A.O.; Kansal, S.K. Visible-Light Driven Photocatalytic Degradation of Brilliant Green Dye Based on Cobalt Tungstate ($CoWO_4$) Nanoparticles. *Mater. Chem. Phys.* **2018**, *211*, 335–342. [CrossRef]
12. Karthikeyan, C.; Arunachalam, P.; Ramachandran, K.; Al-Mayouf, A.M.; Karuppuchamy, S. Recent Advances in Semiconductor Metal Oxides with Enhanced Methods for Solar Photocatalytic Applications. *J. Alloys Compd.* **2020**, *828*, 154281. [CrossRef]
13. Chawla, H.; Chandra, A.; Ingole, P.P.; Garg, S. Recent Advancements in Enhancement of Photocatalytic Activity Using Bismuth-Based Metal Oxides Bi2MO6 (M = W, Mo, Cr) for Environmental Remediation and Clean Energy Production. *J. Ind. Eng. Chem.* **2021**, *95*, 1–15. [CrossRef]
14. Ikram, M.; Rashid, M.; Haider, A.; Naz, S.; Haider, J.; Raza, A.; Ansar, M.T.; Uddin, M.K.; Ali, N.M.; Ahmed, S.S.; et al. A Review of Photocatalytic Characterization, and Environmental Cleaning, of Metal Oxide Nanostructured Materials. *Sustain. Mater. Technol.* **2021**, *30*, e00343. [CrossRef]

15. Lin, J.; Lin, J.; Zhu, Y. Controlled Synthesis of the $ZnWO_4$ Nanostructure and Effects on the Photocatalytic Performance. *Inorg. Chem.* **2007**, *46*, 8372–8378. [CrossRef] [PubMed]
16. Bai, X.; Wang, L.; Zhu, Y. Visible Photocatalytic Activity Enhancement of ZnWO4 by Graphene Hybridization. *ACS Catal.* **2012**, *2*, 2769–2778. [CrossRef]
17. Ke, J.; Niu, C.; Zhang, J.; Zeng, G. Significantly Enhanced Visible Light Photocatalytic Activity and Surface Plasmon Resonance Mechanism of Ag/AgCl/$ZnWO_4$ Composite. *J. Mol. Catal. A Chem.* **2014**, *395*, 276–282. [CrossRef]
18. Dong, T.; Li, Z.; Ding, Z.; Wu, L.; Wang, X.; Fu, X. Characterizations and Properties of Eu3+-Doped ZnWO4 Prepared via a Facile Self-Propagating Combustion Method. *Mater. Res. Bull.* **2008**, *43*, 1694–1701. [CrossRef]
19. Zhang, X.; Wang, B.; Wang, X.; Xiao, X.; Dai, Z.; Wu, W.; Zheng, J.; Ren, F.; Jiang, C. Preparation of M@BiFeO3 Nanocomposites (M = Ag, Au) Bowl Arrays with Enhanced Visible Light Photocatalytic Activity. *J. Am. Ceram. Soc.* **2015**, *98*, 2255–2263. [CrossRef]
20. Wang, F.; Li, W.; Gu, S.; Li, H.; Liu, X.; Wang, M. Fabrication of FeWO4@ZnWO4/ZnO Heterojunction Photocatalyst: Synergistic Effect of $ZnWO_4$/ZnO and $FeWO_4$@$ZnWO_4$/ZnO Heterojunction Structure on the Enhancement of Visible-Light Photocatalytic Activity. *ACS Sustain. Chem. Eng.* **2016**, *4*, 6288–6298. [CrossRef]
21. Li, P.; Zhao, X.; Jia, C.J.; Sun, H.; Sun, L.; Cheng, X.; Liu, L.; Fan, W. ZnWO4/BiOI Heterostructures with Highly Efficient Visible Light Photocatalytic Activity: The Case of Interface Lattice and Energy Level Match. *J. Mater. Chem. A Mater.* **2013**, *1*, 3421–3429. [CrossRef]
22. Mgidlana, S.; Nyokong, T. Asymmetrical Zinc(II) Phthalocyanines Cobalt Tungstate Nanomaterial Conjugates for Photodegradation of Methylene Blue. *J. Photochem. Photobiol. A Chem.* **2021**, *418*, 113421. [CrossRef]
23. Siriwong, P.; Thongtem, T.; Phuruangrat, A.; Thongtem, S. Hydrothermal Synthesis, Characterization, and Optical Properties of Wolframite ZnWO4 Nanorods. *Crystengcomm* **2011**, *13*, 1564–1569. [CrossRef]
24. Pavithra, N.S.; Nagaraju, G.; Patil, S.B. Ionic Liquid-Assisted Hydrothermal Synthesis of $ZnWO_4$ Nanoparticles Used for Photocatalytic Applications. *Ionics* **2021**, *27*, 3533–3541. [CrossRef]
25. Han, S.; Xiao, K.; Liu, L.; Huang, H. $Zn_{1-x}Co_xWO_4$ ($0 \leq x \leq 1$) Full Range Solid Solution: Structure, Optical Properties, and Magnetism. *Mater. Res. Bull.* **2016**, *74*, 436–440. [CrossRef]
26. Rahmani, M.; Sedaghat, T. Nitrogen-Doped ZnWO4 Nanophotocatalyst: Synthesis, Characterization and Photodegradation of Methylene Blue under Visible Light. *Res. Chem. Intermed.* **2019**, *45*, 5111–5124. [CrossRef]
27. Rahmani, M.; Sedaghat, T. A Facile Sol–Gel Process for Synthesis of $ZnWO_4$ Nanopartices with Enhanced Band Gap and Study of Its Photocatalytic Activity for Degradation of Methylene Blue. *J. Inorg. Organomet. Polym. Mater.* **2019**, *29*, 220–228. [CrossRef]
28. Scherrer, P. Estimation of the Size and Internal Structure of Colloidal Particles by Means of Rontgen Rays. *Nachr. Ges. Wiss. Göttingen* **1918**, *26*, 98–100.
29. Tauc, J. *Optical Properties of Solids*; Abelès, F., Ed.; Elsevier: Amsterdam, The Netherlands, 1970.
30. Sadeghfar, F.; Zalipour, Z.; Taghizadeh, M.; Taghizadeh, A.; Ghaedi, M. Photodegradation Processes. *Interface Sci. Technol.* **2021**, *32*, 55–124. [CrossRef]
31. Li, X.; Yu, J.; Low, J.; Fang, Y.; Xiao, J.; Chen, X. Engineering Heterogeneous Semiconductors for Solar Water Splitting. *J. Mater. Chem. A Mater.* **2015**, *3*, 2485–2534. [CrossRef]
32. Fujito, H.; Kunioku, H.; Kato, D.; Suzuki, H.; Higashi, M.; Kageyama, H.; Abe, R. Layered Perovskite Oxychloride Bi4NbO8Cl: A Stable Visible Light Responsive Photocatalyst for Water Splitting. *J. Am. Chem. Soc.* **2016**, *138*, 2082–2085. [CrossRef]
33. Li, Y.; Hua, S.; Zhou, Y.; Dang, Y.; Cui, R.; Fu, Y. Activating $ZnWO_4$ Nanorods for Efficient Electroanalysis of Bisphenol A via the Strategy of In Doping Induced Band Gap Change. *J. Electroanal. Chem.* **2020**, *856*, 113613. [CrossRef]
34. Yu, X.; Williams, C.T. Recent Advances in the Applications of Mesoporous Silica in Heterogeneous Catalysis. *Catal. Sci. Technol.* **2022**, *12*, 5765–5794. [CrossRef]
35. Malik, J.; Kumar, S.; Srivastava, P.; Bag, M.; Mandal, T.K. Cation Disorder and Octahedral Distortion Control of Internal Electric Field, Band Bending and Carrier Lifetime in Aurivillius Perovskite Solid Solutions for Enhanced Photocatalytic Activity. *Mater. Adv.* **2021**, *2*, 4832–4842. [CrossRef]
36. Kirankumar, V.S.; Sumathi, S. Copper and Cerium Co-Doped Cobalt Ferrite Nanoparticles: Structural, Morphological, Optical, Magnetic, and Photocatalytic Properties. *Environ. Sci. Pollut. Res.* **2019**, *26*, 19189–19206. [CrossRef] [PubMed]
37. Pan, Y.M.; Zhang, W.; Hu, Z.F.; Feng, Z.Y.; Ma, L.; Xiong, D.P.; Hu, P.J.; Wang, Y.H.; Wu, H.Y.; Luo, L. Synthesis of Ti^{4+}-Doped $ZnWO_4$ Phosphors for Enhancing Photocatalytic Activity. *J. Lumin.* **2019**, *206*, 267–272. [CrossRef]
38. Otrokov, M.M.; Klimovskikh, I.I.; Calleja, F.; Shikin, A.M.; Vilkov, O.; Rybkin, A.G.; Estyunin, D.; Muff, S.; Dil, J.H.; Vázquez De Parga, A.L.; et al. Evidence of Large Spin-Orbit Coupling Effects in Quasi-Free-Standing Graphene on Pb/Ir(1 1 1). *2d Mater* **2018**, *5*, 035029. [CrossRef]
39. Magdalane, C.M.; Kaviyarasu, K.; Vijaya, J.J.; Siddhardha, B.; Jeyaraj, B.; Kennedy, J.; Maaza, M. Evaluation on the Heterostructured CeO_2/Y_2O_3 Binary Metal Oxide Nanocomposites for UV/Vis Light Induced Photocatalytic Degradation of Rhodamine–B Dye for Textile Engineering Application. *J. Alloys Compd.* **2017**, *727*, 1324–1337. [CrossRef]
40. Zheng, X.; Yuan, J.; Shen, J.; Liang, J.; Che, J.; Tang, B.; He, G.; Chen, H. A Carnation-like RGO/$Bi_2O_2CO_3$/BiOCl Composite: Efficient Photocatalyst for the Degradation of Ciprofloxacin. *J. Mater. Sci. Mater. Electron.* **2019**, *30*, 5986–5994. [CrossRef]
41. Balu, S.; Velmurugan, S.; Palanisamy, S.; Chen, S.W.; Velusamy, V.; Yang, T.C.K.; El-Shafey, E.S.I. Synthesis of α-Fe_2O_3 Decorated g-C_3N_4/ZnO Ternary Z-Scheme Photocatalyst for Degradation of Tartrazine Dye in Aqueous Media. *J. Taiwan Inst. Chem. Eng.* **2019**, *99*, 258–267. [CrossRef]

42. Naresh, G.; Malik, J.; Meena, V.; Mandal, T.K. PH-Mediated Collective and Selective Solar Photocatalysis by a Series of Layered Aurivillius Perovskites. *ACS Omega* **2018**, *3*, 11104–11116. [CrossRef] [PubMed]
43. Saher, R.; Hanif, M.A.; Mansha, A.; Javed, H.M.A.; Zahid, M.; Nadeem, N.; Mustafa, G.; Shaheen, A.; Riaz, O. Sunlight-Driven Photocatalytic Degradation of Rhodamine B Dye by Ag/$FeWO_4$/g-C_3N_4 Composites. *Int. J. Environ. Sci. Technol.* **2021**, *18*, 927–938. [CrossRef]
44. Zhang, P.; Liang, H.; Liu, H.; Bai, J.; Li, C. A Novel Z-Scheme BiOI/BiOCl Nanofibers Photocatalyst Prepared by One-Pot Solvothermal with Efficient Visible-Light-Driven Photocatalytic Activity. *Mater. Chem. Phys.* **2021**, *272*, 125031. [CrossRef]
45. Santana, R.W.R.; Lima, A.E.B.; de Souza, L.K.C.; Santos, E.C.S.; Santos, C.C.; de Menezes, A.S.; Sharma, S.K.; Cavalcante, L.S.; Maia da Costa, M.E.H.; Sales, T.O.; et al. BiOBr/$ZnWO_4$ Heterostructures: An Important Key Player for Enhanced Photocatalytic Degradation of Rhodamine B Dye and Antibiotic Ciprofloxacin. *J. Phys. Chem. Solids* **2023**, *173*, 111093. [CrossRef]
46. Geetha, G.V.; Sivakumar, R.; Slimani, Y.; Sanjeeviraja, C.; Kannapiran, E. Rare Earth (RE: La and Ce) Elements Doped $ZnWO_4$ Nanoparticles for Enhanced Photocatalytic Removal of Methylene Blue Dye from Aquatic Environment. *Phys. B Condens. Matter* **2022**, *639*, 414028. [CrossRef]
47. Liu, X.; Shu, J.; Wang, H.; Jiang, Z.; Xu, L.; Liu, C. One-Pot Preparation of a Novel CoWO4/ZnWO4 p-n Heterojunction Photocatalyst for Enhanced Photocatalytic Activity under Visible Light Irradiation. *J. Phys. Chem. Solids* **2023**, *172*, 111061. [CrossRef]
48. Kumar, G.M.; Lee, D.J.; Jeon, H.C.; Ilanchezhiyan, P.; Deuk Young, K.; Tae Won, K. One Dimensional $ZnWO_4$ Nanorods Coupled with WO_3 Nanoplates Heterojunction Composite for Efficient Photocatalytic and Photoelectrochemical Activity. *Ceram. Int.* **2022**, *48*, 4332–4340. [CrossRef]
49. Jaramillo-Páez, C.; Navío, J.A.; Puga, F.; Hidalgo, M.C. Sol-Gel Synthesis of $ZnWO_4$-(ZnO) Composite Materials. Characterization and Photocatalytic Properties. *J. Photochem. Photobiol. A Chem.* **2021**, *404*, 112962. [CrossRef]
50. Jayamani, G.; Shanthi, M. An Efficient Nanocomposite CdS-$ZnWO_4$ for the Degradation of Naphthol Green B Dye under UV-A Light Illumination. *Nano-Struct. Nano-Objects* **2020**, *22*, 100452. [CrossRef]
51. Geetha, G.V.; Keerthana, S.P.; Madhuri, K.; Sivakumar, R. Effect of Solvent Volume on the Properties of $ZnWO_4$ Nanoparticles and Their Photocatalytic Activity for the Degradation of Cationic Dye. *Inorg. Chem. Commun.* **2021**, *132*, 108810. [CrossRef]

Disclaimer/Publisher's Note: The statements, opinions and data contained in all publications are solely those of the individual author(s) and contributor(s) and not of MDPI and/or the editor(s). MDPI and/or the editor(s) disclaim responsibility for any injury to people or property resulting from any ideas, methods, instructions or products referred to in the content.